V International Conference on Simulation for Additive Manufacturing
Sim-AM 2025
F. Auricchio, M. Carraturo and S. Morganti (Eds)

SHAPE OPTIMIZATION OF THIN-WALLED GEOMETRIES FOR LAYER-BASED DIRECT DEPOSITION ADDITIVE MANUFACTURING

FABIA SCHITO[*†‡], JESUS DANIEL MEZA ZERON[†], KATHRIN DÖRFLER[*], PIERLUIGI D'ACUNTO[†], MAJID HOJJAT[‡]

[*]Professorship of Digital Fabrication, Technical University of Munich
Arcisstrasse 21, 80333 München
e-mail: fabia.schito@bmw.de, doerfler@tum.de

[†]Professorship of Structural Design, Technical University of Munich
Arcisstrasse 21, 80333 München
e-mail: daniel.meza@tum.de, pierluigi.dacunto@tum.de

[‡]BMW AG
Bremer Str. 6, 80807 München
e-mail: majid.hojjat@bmw.de

Key words: numerical simulations, Additive Manufacturing (AM), computational modeling

Abstract. In layer-based direct deposition Additive Manufacturing (AM), the geometry of thin-walled structures fits particularly well with path-planning methods, where the print head's movement is optimized to follow continuous deposition paths. Despite this potential, reliably assessing the printability of such structures and embedding these assessments into computational design optimization remains a challenge. To address this gap, we propose a Shape Optimization (SO) Method based on surface energies that modifies an existing surface-based geometry, defined within prescribed closed boundary curves, to enhance the printability of the given design while preserving the fixed boundaries. The optimization relies on a scalar field and surface parametrization to introduce a surface energy functional, which models the distribution of isolines corresponding to non-continuous printing paths. Printability is linked to the uniformity of these isoline distributions across the surface, and a fabrication metric is defined to evaluate design feasibility. Sensitivity analysis is performed with automatic differentiation, combined with spectral filtering regularization, and optimization is carried out in a nested loop for both the parametric field and the shape. The outcome is a surface-based design with improved fabrication feasibility for layer-based direct deposition AM, along with the corresponding isolines that define the printing paths. The method is demonstrated on different geometries, including an industrial case, and validated using Fused Deposition Modeling (FDM).

1 INTRODUCTION

1.1 Application, Motivation and Framework

In the realm of industrial product design, Shape Optimization based only on path-planning can enhance printability for layer-based direct deposition Additive Manufacturing (AM) processes, which encompass Fused Deposition Modeling (FDM), Wire Arc Additive Manufacturing (WAAM), concrete, and clay 3D printing. In this framework, using smooth and continuous surfaces within pre-

scribed boundaries is highly beneficial for material and geometry complexity reduction. For these shapes, non-planar printing-paths are advantageous, as they allow for boundaries preservation, avoiding further post-processing manufacturing operations. Additionally, they reduce the staircase effect, since the non-planarity accommodates the layer directly onto the desired surface, minimizing slicing approximation of the shape, especially when combined with layer-orthogonal-printing orientation. Moreover, they lessen the need for supports since each layer conforms to the surface and can achieve a greater interlayer contact area than conventional planar printing. Furthermore, they improve surface quality, thanks to the higher degrees of freedom in adapting to the desired shape in a 3D space, and enhance continuous 3D printing-paths, by simplifying the spiralization procedure from non-continuous sets of printing-paths.

1.2 Challenges, Research Question and Proposal

Two main challenges can be highlighted in this context. First, for a given 3D surface it is non-trivial to define an optimal path-height distribution, such that it is smooth, continuous within the layer, minimizes support structures, captures all the geometrical features, or generally suits some desired path-planning properties. Secondly, it is often the case that, even for an optimal path-distribution, the non-planar path-planning strategy may be incompatible with the specific machine capabilities (e.g. dimension of the nozzle and expansion properties of the material), which means that the design feasibility must be checked against machine layer-height constraints. In fact, by operating within a layer-height range, the planned path and therefore the computed layer-height h must fit into the limits of the minimum (h_L) and maximum (h_U) layer-height printable by the specific machine (Figure 1).

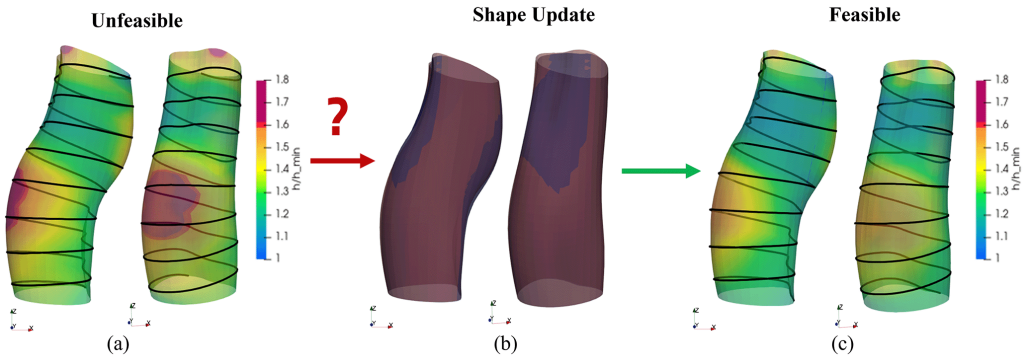

Figure 1: Research Question. (a) On an initial surface geometry, a printing-path and layer-height distribution are derived. By considering the deposition modulation m, the feasibility condition can be expressed as $m = h/h_{min} < h_U/h_L$. In this setup, areas with $m > 1.6$ are considered unfeasible. (b) The initial surface (dark blue) must therefore be updated (dark red) such that the shape can become feasible. (c) The optimized shape and printing-path respect the lower (h_L) and upper (h_U) layer-height boundaries. Feasibility is reflected by the absence of regions with $m > 1.6$.

Therefore, our research question states: given an initial geometry, how can we simultaneously optimize both the shape and the printing path for layer-based direct deposition AM?

To optimize path-height distribution, we propose the usage of non-planar evenly spaced printing-paths within machine limits (h_L, h_U). To bridge the gap between design feasibility and machine constraints, we realize a coupled nested-loop optimization where both shape and printing-paths inform each other iteratively. The full workflow is schematized in Figure 2.

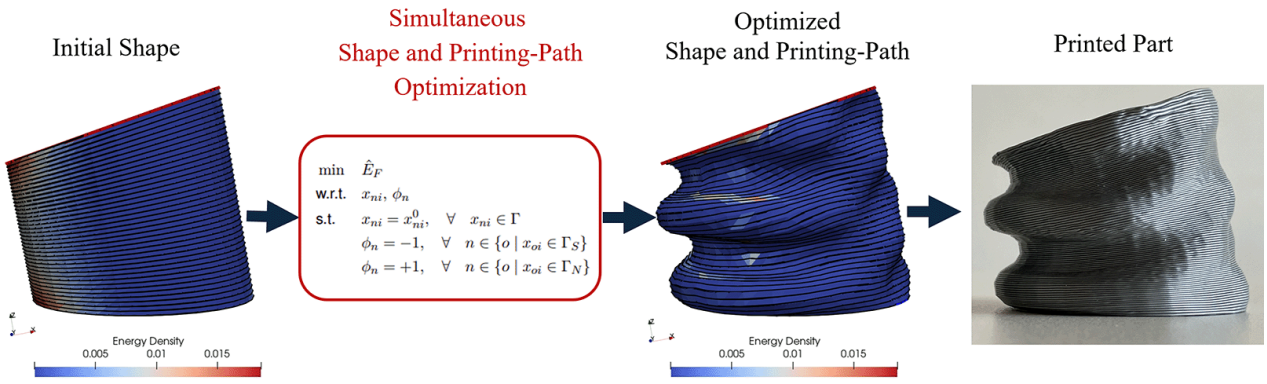

Figure 2: Workflow Overview. On an initial shape, a path-distribution is realized and a feasibility metric called *energy density* E_F allows to identify the non-feasible area (red) and serves as a foundation for a Simultaneous Shape and Printing-Path optimization preserving the boundaries. The optimized shape is now printable.

2 STATE OF THE ART

Path-planning and relative optimization have been successfully explored for different layer-based direct deposition AM technologies. Although surface informed, no shape modification is considered in these applications. Some attempts in performing shape optimization tailored to manufacturability have been proven promising for improving build direction [1] and respecting feature size, but path-planning has not been considered as a main parameter. Topology optimization, on the other hand, has been widely explored in relation to manufacturing constraints such as build orientation [2], but also – closer to path-planning – to space-time fabrication sequence and deposit direction [3]. However, 3D surfaces are typically not addressed. There is, therefore, still a substantial gap in developing co-design approaches that simultaneously optimize shape and fabrication path-planning.

3 METHODOLOGY

We present our method for simultaneous shape and printing-path optimization of thin-walled structures. The full detailed pipeline is depicted in Figure 3, and the optimization implementation is described by Figure 4.

3.1 Assumptions

From a geometric perspective, we define the shape design space as a 2-manifold with boundaries embedded in the Euclidean space $\mathbb{R}^3$. This space represents thin-walled structures that can be printed using a single bead. In a discrete setting, this design space is represented by a 2-simplicial complex, specifically a triangle mesh.

From a printing-path-manufacturing perspective, we adopt a purely geometrical approach, without any structural, thermal analysis or any other complex aspects. As the layering conveys the most important information about fabrication, it is therefore the only fabrication parameter considered in the optimization. The manufacturability objective translates the need for equally spaced layers and therefore the feasibility condition must ensure that the local layer-height h is within the machine capability, i.e. $h_L \leq h \leq h_U$. We assume that the modulation capability condenses the relevant machine limitations and is defined as $\eta = h_U/h_L$. Furthermore, the layer is considered with a circular cross-section and treated as 3D polyline, and a node-based shape optimization allows for more design freedom.

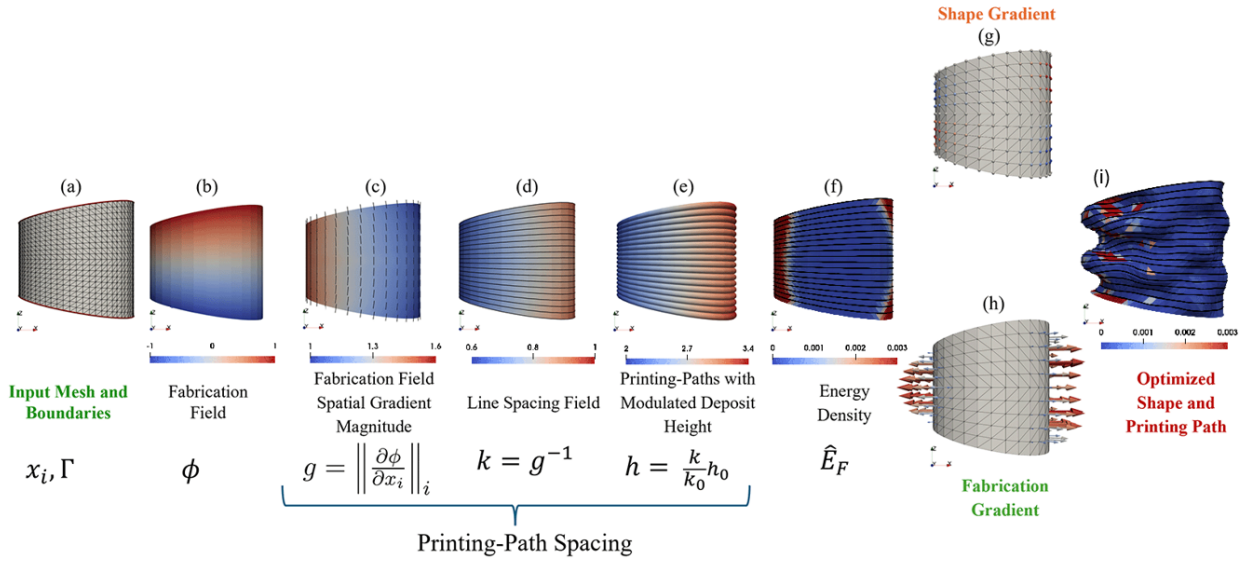

Figure 3: Full Workflow. The shape optimization problem starts with the input mesh and boundaries. A fabrication field is defined, which simply acts as a surface paramterization. The printing-path spacing is then computed in three main steps and a functinoal named Energy Density is computed. Sensitivities finally allow for the shape a printing-paths updates. The method is independent from any base-plate orientation. The base-plate reference frame is highlighted only for the final step, where it is fundamental.

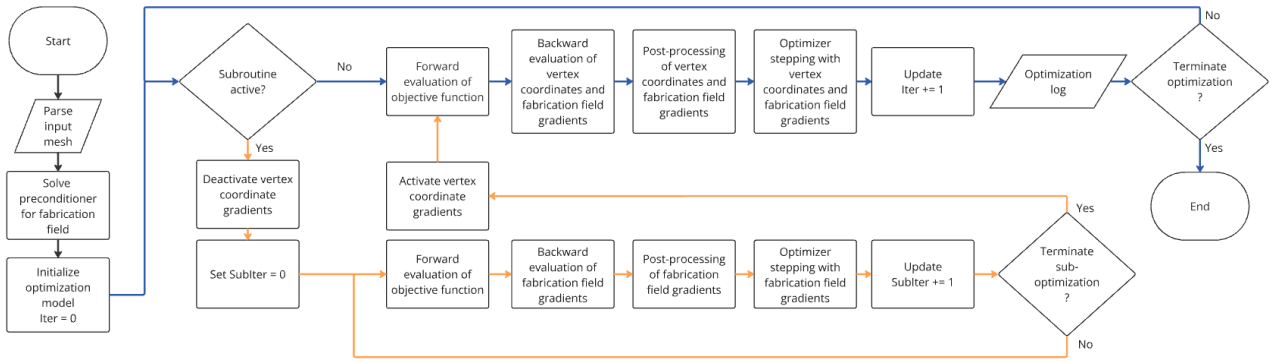

Figure 4: Optimization loops. The nested loop optimization allows for the definition of the optimal printing-path for the current iteration (orange) according to fabrication gradient, and successively for the update of the shape according to shape gradients (blue).

3.2 Scalar-Field-Based Path-Planning

As in existing approaches [4], given an initial surface with start and end boundaries of the printing (Figure 3a), we use a vertex-based scalar field (Figure 3b) to represent printing-paths on a thin-walled surface Ω (Figure 3e). This mesh attribute, denoted as the fabrication field ϕ and defined at the nodes x_n, describes printing-paths as non-intersecting level sets:

$$s(\hat{\phi}) = \{x_i \in \Omega \mid \phi(x_i) = \hat{\phi}\} \tag{1}$$

The fabrication field acts as an interpolator, between Start and End boundaries of the printing ($\phi_S = -1, \phi_N = +1$) and it adapts to the number of printing-paths by resampling them. It provides information on deposit height and it bridges the spatial geometric space and the fabrication space

(Figure 5). As a consequence, it allows to derive printing-paths which lie on the surface to preserve shape fidelity and interpolate between given start and end boundaries to enforce boundary conformity. Furthermore, they do not intersect to prevent material overlap or collisions, and they are continuous within the layer to ensure trajectory integrity and discontinuous across the surface. Spiralization can be performed in post-processing through linearization of subsequent isolines, which are non-planar to adapt to the boundary curves without staircasing them. Additionally, from a computational perspective, our approach represents printing paths as two types of information: (1) spatial deposition trajectory, meaning the geometric course of the nozzle as it moves across the surface, and (2) material deposition modulation, meaning the local variation in the amount of material deposited along that path. In the optimization, the nozzle is always assumed to remain tangential to the surface; only the frame orientation around the nozzle's vertical axis (z-axis rotation) is excluded. Both trajectory and modulation are derived directly from the scalar field ϕ and stored as nodal values on the surface.

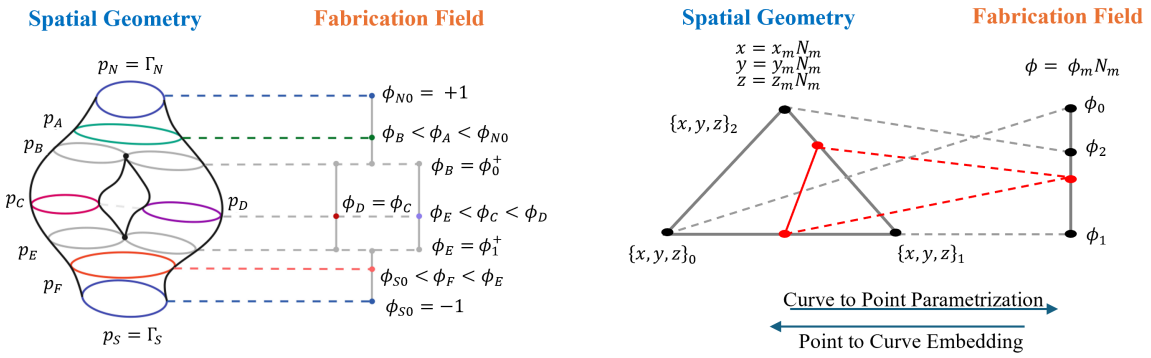

Figure 5: Correspondence between Spatial Geometry and Fabrication Field. Global geometry representation (left), element representation (right). Each path-isoline p corresponds to a single scalar value of the fabrication field ϕ. The points of the geometries where the gradient of the fabrication field vanishes are the singularity points, where more than a single isoline corresponds to one ϕ^* value. Those points identify a branch splitting/rejoining and allow for skeletonization of the 3D surface. Since triangular elements with linear shape functions are used, a line within the element of the mesh corresponds to a point in the fabrication field, and equidistant isolines within the element correspond to equispaced points of the fabrication field.

Continuity of the path is ensured by interpolating vertex values of ϕ using barycentric shape functions ξ, η, in the same manner as vertex coordinates are usually interpolated:

$$x_i(m, \xi, \eta) = \sum_n x_{ni} N_n(m, \xi, \eta) \tag{2}$$

$$\phi(m, \xi, \eta) = \sum_n \phi_n N_n(m, \xi, \eta) \tag{3}$$

Boundary-conforming printing-paths are enforced by prescribing constant values at the boundaries:

$$\phi_n = \phi_A, \quad \forall x_{ni} \in \Gamma_A \tag{4}$$

The interior values of the fabrication field are then computed to smoothly interpolate the prescribed boundary constraints. Common choices include harmonic or biharmonic functions [5], which solve for interior values based on boundary conditions and can serve as effective preconditioners for the fabrication field.

A path following the gradient direction (Figure 3c) of ϕ moves orthogonally to the contours. The distance between two such points $x_i(\phi_0)$ and $x_i(\phi_1)$ along the path is:

$$h = \int_{\phi_0}^{\phi_1} \left\| \frac{\partial x_i}{\partial \phi} \right\|_2 d\phi = \int_{\phi_0}^{\phi_1} \left\| \frac{\partial \phi}{\partial x_i} \right\|_2^{-1} d\phi \tag{5}$$

For level sets $s(\hat{\phi}_i)$ spaced at constant intervals $\Delta\hat{\phi}$, the inverse gradient magnitude $k = \left\| \frac{\partial \phi}{\partial x_i} \right\|_2^{-1}$ indicates the local printing-path spacing (Figure 3d). From this printing-paths can be extrapolated as isolines and the modulated deposit height computed (Figure 3e).

3.3 Printing-path Feasibility

While the fabrication field approach yields continuous, non-intersecting, and boundary-conforming printing-path, it does not inherently ensure fabrication feasibility. In practice, the deposition height h is limited by machine-specific bounds $h \in [h_L, h_U]$. To capture the machine's ability to modulate print height, we define the modulation capability ratio as:

$$\eta = \frac{h_L}{h_U} \tag{6}$$

The modulation capability converts the line-spacing field k into a density distribution acting as a converter from shape to printing path information. Since printing-path spacing is proportional to the inverse gradient magnitude of the fabrication field, the spacing constraint thus translates to:

$$k \in [k_L, k_U] \tag{7}$$

Assuming a mean-centered, symmetric distribution of k over the domain Ω, we define the following relations:

$$A = \int_\Omega d\omega \approx \sum_m A_m \tag{8}$$

$$\bar{k} = \frac{1}{A} \int_\Omega k \, d\omega \approx \frac{1}{A} \sum_m k_m A_m \tag{9}$$

$$k_L = \bar{k} \left(1 - \frac{\eta - 1}{\eta + 1} \right) \tag{10}$$

$$k_U = \bar{k} \left(1 + \frac{\eta - 1}{\eta + 1} \right) \tag{11}$$

where A_m is the area and k_m the inverse gradient magnitude of the fabrication field at face m. As we use bilinear finite elements, the gradient is constant within the element, which results in constant line spacing at each face. For an arbitrary fabrication field, the values $k(x_i) \in \mathbb{R}^+$ may violate the feasible bounds. To quantify this deviation and enable optimization, we introduce an objective function E penalizing values outside $[k_L, k_U]$, suitable for use in gradient-based optimization. Areas below or over the feasible bounds would require respectively an over or under deposition of material to be manufactured (e.g. due to nozzle size), while areas within the limits can be printed by exploiting the full layer-height range of the machine (Figure 6).

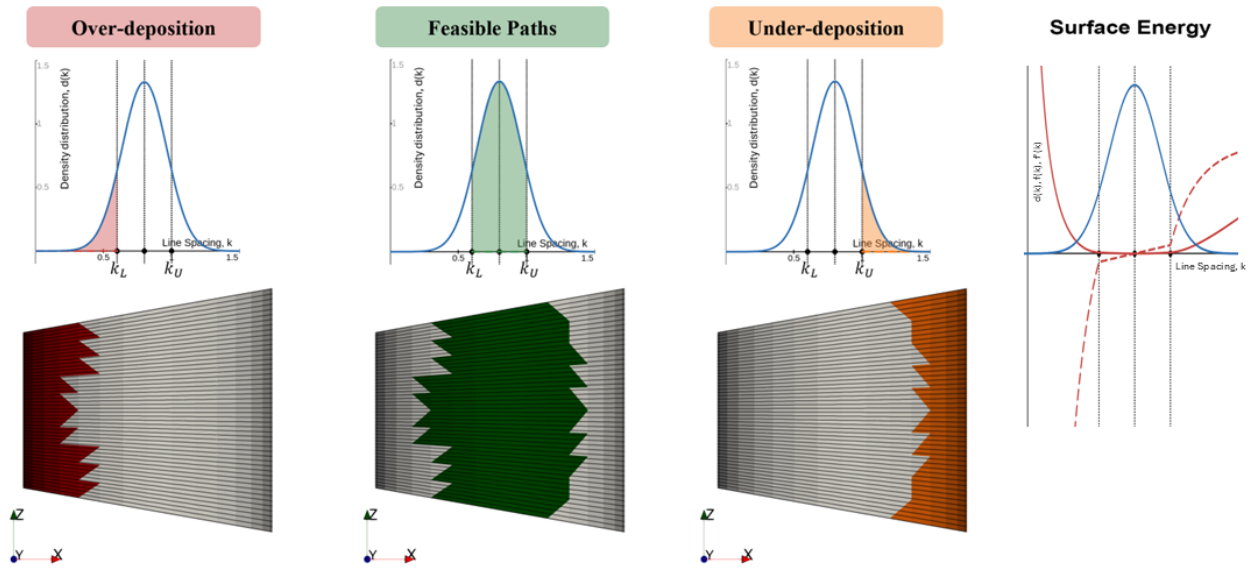

Figure 6: Feasible, over and under deposition areas according to the machine layer-height constraints k_L and k_U (left). Modulation Surface Energy functional (right). Density distribution (blue), surface energy density (red), modulation surface energy function (dashed red).

3.4 Modulation Surface Energy

To enable gradient-based optimization methods, we define a surface energy functional that penalizes local deviations from feasible printing-path spacing. This energy is aggregated by integrating a surface energy density $f(k)$ over the domain, to compute the *Modulation Surface Energy* as:

$$E_F = \int_\Omega f(k)\, d\omega \approx \sum_m \{f(k)\}_m\, A_m \tag{12}$$

Since k is strictly positive, we define the energy density $f(k)$ in logarithmic scale to symmetrically penalize squared deviations from the global mean $\bar{k}$:

$$f(k) = (ln(\bar{k}) - ln(k))^2 = \bar{k}^2 ln^2\left(\frac{\bar{k}}{k}\right) \tag{13}$$

where $\bar{k}^2$ is used for global rescaling to ensure that $f''(k = \bar{k})$ remains constant. The logarithmic scale is also necessary to handle singular points where the gradient magnitude approaches zero and, therefore, $k \to \infty$. Notice that while $f(k) \to \infty$ as $k \to \infty$, the gradients remain stable at singular points, with $f'(k) \to 0$.

This expression results in a surface energy equal to zero only when all spacing values are equal. However, such a hard constraint does not fully utilize the machine's modulation capability. To allow bounded variation in k within the feasible range $[k_L, k_U]$, we apply a piecewise rescaling using min and max operators:

$$\tilde{k}_m = \frac{\bar{k}}{k_L}\left[\min(k_m, k_L) + \max(k_m, k_U) - k_U\right] \tag{14}$$

This transformation neglects contributions from values within the feasible range while penalizing those outside it. The final surface energy (Figure 6, right) is then evaluated as:

$$E_F = \int_\Omega f(\tilde{k}) d\omega \approx \sum_m \{f(\tilde{k})\}_m A_m \tag{15}$$

3.5 The Optimization Problem

The optimization problem is formulated as following:

$$\begin{aligned} \min \quad & \hat{E}_F \\ \text{w.r.t.} \quad & x_{ni}, \phi_n \\ \text{s.t.} \quad & x_{ni} = x_{ni}^0 \\ & \phi_n = -1, \quad \forall\, n \in \{o \mid x_{oi} \in \Gamma_S\} \\ & \phi_n = +1, \quad \forall\, n \in \{o \mid x_{oi} \in \Gamma_N\} \end{aligned} \tag{16}$$

It is solved with gradient steepest descent, optimizing internally to the loop for the design variables ϕ_n and externally for x_{ni} as shown in Figure 4. The surface energy is generally non-zero (Figure 3f), until the problem converges.

3.6 Sensitivity Analysis

Due to the algebraic complexity of computing gradients in geometric embeddings, we rely on Automatic Differentiation (AD) to obtain sensitivities (Figure 7). AD provides exact gradients and allows implementation using standard computational frameworks. For this to be possible, the evaluation of the *Modulation Surface Energy* must be expressed as a forward pass through a computational graph. This structure enables efficient backward evaluation of the gradients with respect to both spatial (Figure 3g) and fabrication (Figure 3h) design variables:

$$\frac{\partial E_F}{\partial x_{ni}} \quad \text{(w.r.t. vertex spatial coordinates)} \tag{17}$$

$$\frac{\partial E_F}{\partial \phi_n} \quad \text{(w.r.t. vertex fabrication values)} \tag{18}$$

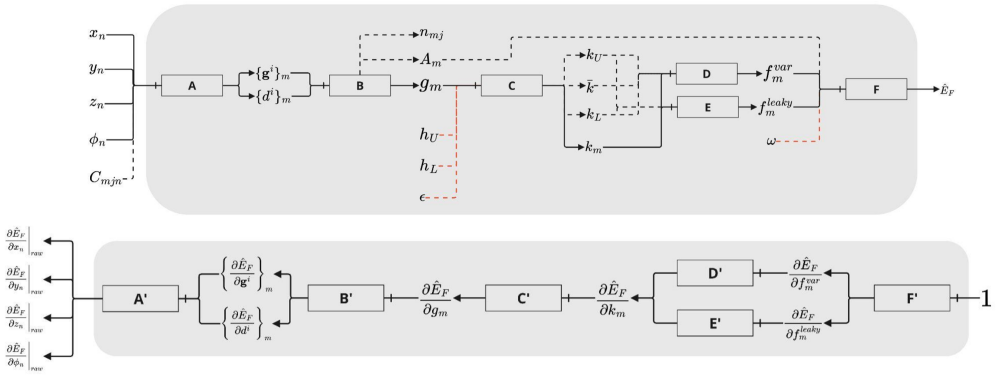

Figure 7: Forward (top) and Backward (bottom) AD pass for sensitivities computation.

As described in Section 3.4, the energy density and its gradients vanish in regions where $k \in [k_L, k_U]$. While this reflects feasibility, it can lead to stagnation during optimization, as no update is driven in those regions. To address this, we introduce a *leaky energy density* that supplements the original energy with a small, non-zero gradient within the feasible range, and constant gradients

outside of the feasible range:

$$f^{leaky}(k) = \begin{cases} k(k_L - k_U) + C_0, & \text{if } k < k_L \\ (k - C_1)^2, & \text{if } k_L \leq k \leq k_U \\ k(k_U - k_L) + C_2, & \text{if } k > k_U \end{cases} \tag{19}$$

$$C_0 = \frac{1}{4}(k_U^2 + 2k_U k_L - 3k_L^2) \tag{20}$$

$$C_1 = \frac{1}{2}(k_U + k_L) = \bar{k} \tag{21}$$

$$C_2 = \frac{1}{4}(k_L^2 + 2k_L k_U - 3k_U^2) \tag{22}$$

The total energy density is then given by:

$$f^{\text{total}}(k) = f(k) + w f^{leaky}(k) \tag{23}$$

with w controlling the strength of the leaky component.

3.7 Filtering

Particular care must be taken with the representational capacity of the sensitivity fields used to update the shape and printing paths. Triangular meshes with bilinear shape functions yield surface and field representations that are continuous but not differentiable. Without regularization, optimization may lead to sharp discontinuities or low smoothness in both the shape and the printing-paths on it. We mitigate this by applying a spectral filtering. The main goal is to realize a compression of the design variables using a projection and reconstruction as a low-rank approximation for smoothing gradients according to dominant modes. A visual representation is depicted in Figure 8.

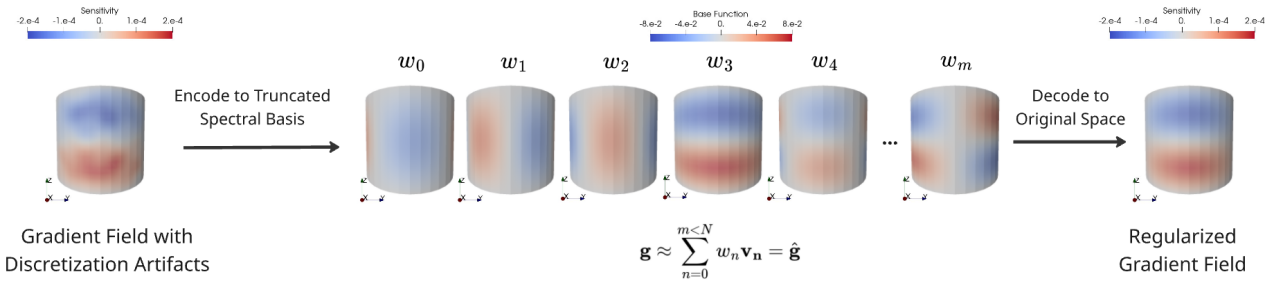

Figure 8: Regularization based on the eigenvectors of the Discrete Laplacian Operator.

The eigenvectors form an orthonormal basis with respect to the Euclidean inner product, analogous to a Hilbert space basis in the continuous setting. This basis provides a change of coordinates for representing the sensitivity fields on which features are ordered depending on their size. To reflect the preservation of boundaries in the optimization steps, the nodes at the boundaries are clamped by adding a stiffness α to them.

$$L^*_{mn} = \begin{cases} L_{mn} + \alpha, & \text{if } m = n \text{ and } x_m \in \Gamma, \\ L_{mn}, & \text{otherwise.} \end{cases} \tag{24}$$

$$\boldsymbol{L}^* = \sum_{n=0}^{N} \lambda_n \boldsymbol{v_n} \otimes \boldsymbol{v_n} \tag{25}$$

where $\boldsymbol{L}$ is the cotangent Laplacian Matrix, $\boldsymbol{L}^*$ the modified Laplacian matrix with clamped boundary nodes and $\boldsymbol{v_n}$ and λ_n its eigenvectors and eigenvalues respectively. The eigenvectors allow an encoding of the sensitivity field as the projection w_n of the gradient $\boldsymbol{g}$ onto the eigenvectors $\boldsymbol{v_n}$ of $\boldsymbol{L}$:

$$w_n = \langle \boldsymbol{g}, \boldsymbol{v_n} \rangle \tag{26}$$

The reconstructed gradient $\hat{\boldsymbol{g}}$ is evaluated through the truncated decoding, on which the features corresponding to the eigenvectors $v_n, n > m$ are removed:

$$\hat{\boldsymbol{g}} = \sum_{n=0}^{m<N} w_n \boldsymbol{v_n} \tag{27}$$

This filtering technique enables some important properties. The results are almost mesh-independent, as they are not influenced by symmetries or uniformity in the tessellation. The refinement still plays a role. Furthermore, the introduction of the hyper-parameters of the eigenvalues into the optimization, allows for a more intuitive control on the optimization, since the number of eigenvalues for shape gradient N_g directly influences the smoothness of the optimized shape (features' size), while the number of eigenvalues for fabrication gradient N_ϕ is responsible of the smoothness of the printing-paths. The full workflow is summarized and shown on the example of a more complex geometry, such as the vase in Figure 9.

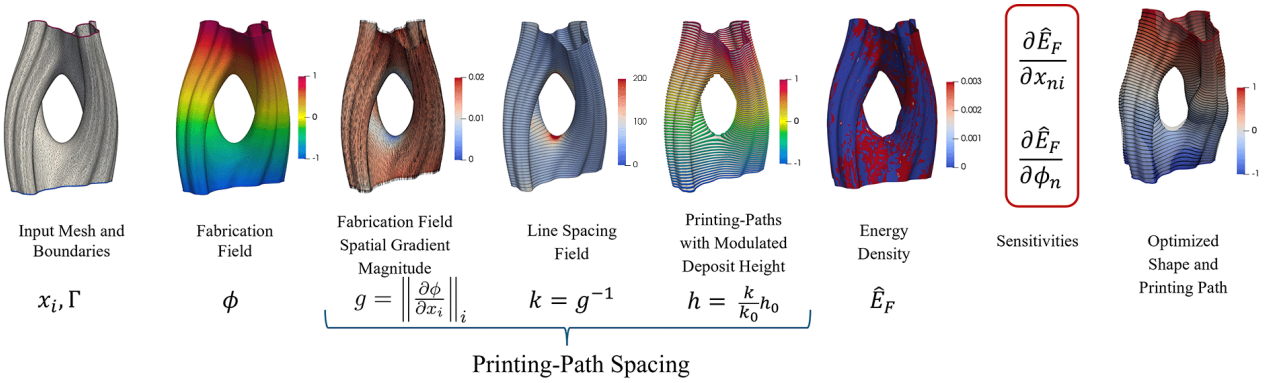

Figure 9: Method Summary. From the input Mesh and Boundaries, the Optimised Shape and Printing Paths are derived for a vase example.

4 RESULTS AND DISCUSSION

The results applied to the example of the skewed cylinder can be seen in Figure 3i. Depending on the modulation capability η, Figure 12 shows that the extent of modifications needed must adapt to the layer-height fabrication constraint, meaning that a nozzle with a higher printability range will require less adaptation of the original design, while for very limited printability range more modifications are needed to homogeneously distribute the paths over the surface, such that the local geodesic distances between subsequent priniting-paths are as uniform as possible considering the machine limitations.

Further examples, including an industrial application, are collected in Figure 11. The method has been validated by printing with FDM the skewed cylinder for $\eta = 1.3$ in Figure 12.

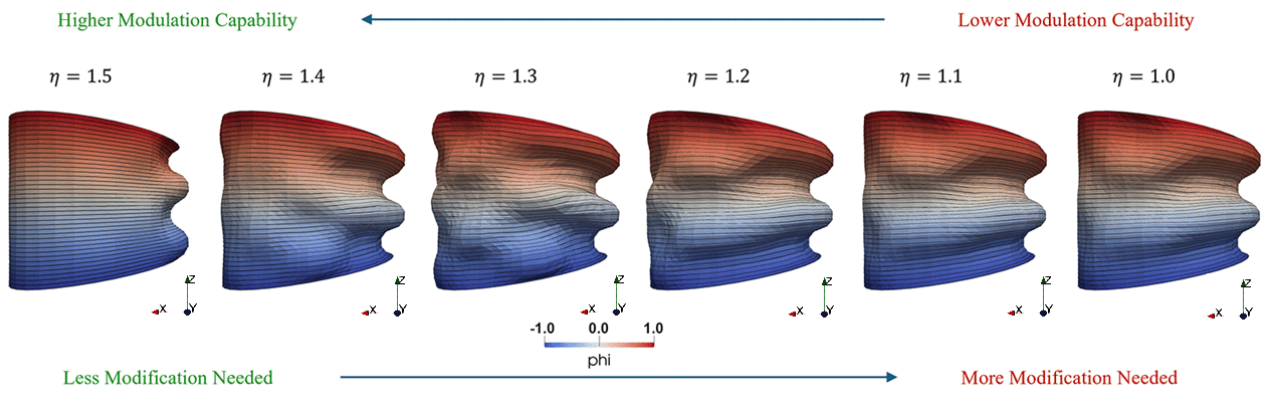

Figure 10: Results on the skewed cylinder for different modulation capability values.

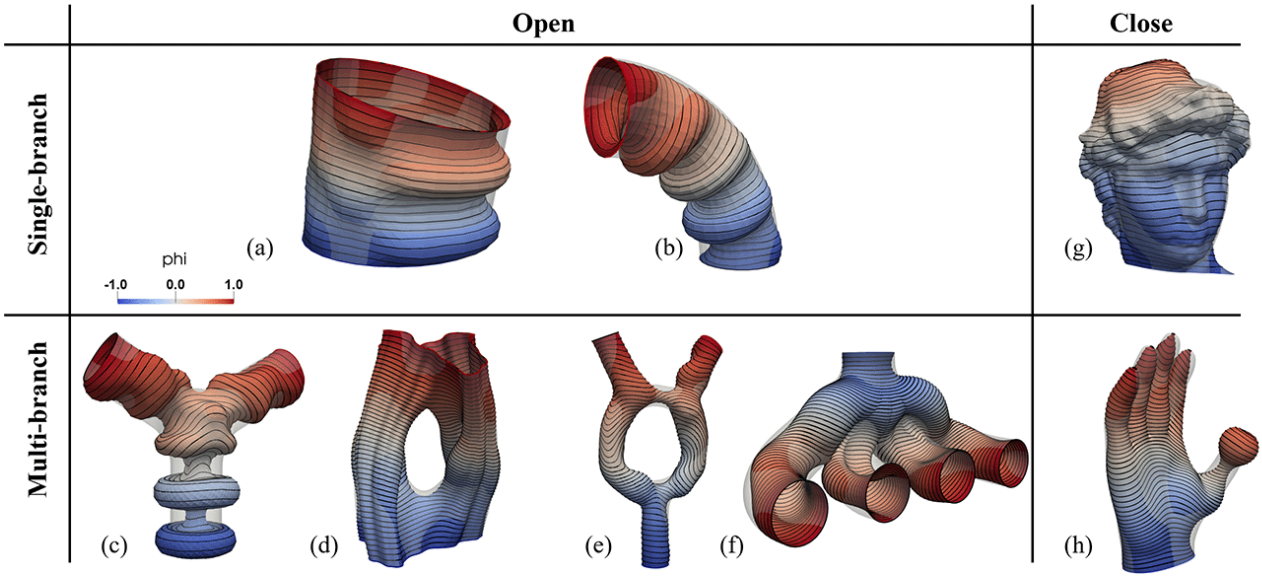

Figure 11: Results. Several examples shows the optimization of single-branch, multi-branch open and close geometries. For multi-branch, more than one segmentation is needed.

5 CONCLUSIONS, LIMITATIONS AND OUTLOOK

We presented a novel methodology that realizes a simultaneous optimization of shape and printing-paths. In our optimization framework, a computational graph enables the evaluation of design gradient fields, while the introduction of a customized filtering allows for the design variable compression achieved through spectral projection of the sensitivities. Manufacturability has been simplified, accounting only for the printing-paths fabricability and aiming at an evenly spaced layer-height distribution within the machine layer-height range expressed as lower (h_L) and upper boundary (h_U). Path-planning feasibility, therefore, has been evaluated using a scalar objective function, named Modulation Surface Energy, which models the uniformity in layer-height all over the surface, accounting for boundary preservation, taking advantage of non-planar printing-path. Key properties of our methodology are the boundary and shape features preservation, and an active smoothness control of both shape and printing-path with the hyperparameters of the eigenvectors number used in the filtering.

Some limitations of the method can be highlighted. Regarding manufacturability, considering

only path-planning and adopting a purely geometrical approach captures only limited aspects of the fabrication. For example, collisions or singular positions in robot kinematics are not perceived by the objective function. Figure 11c, in fact, shows a computationally valid result that, despite minimizing the objective function, may not be manufacturable. The optimization may be critical as we deal with high non-convexity, and we have a gradient post-processing dependency. For topologically complex designs, the hyperparameter tuning process becomes increasingly challenging.

Although we tested the method on a simple geometry, further testing and validation are needed. The manufacturability modeling must be improved with additional fabrication constraints, such as frame orientation, collisions, design space constraints, and more complex physics, such as stress and thermal analysis. The optimization framework that we built, thanks to its modularity, can be easily extended with multiple constraints optimization.

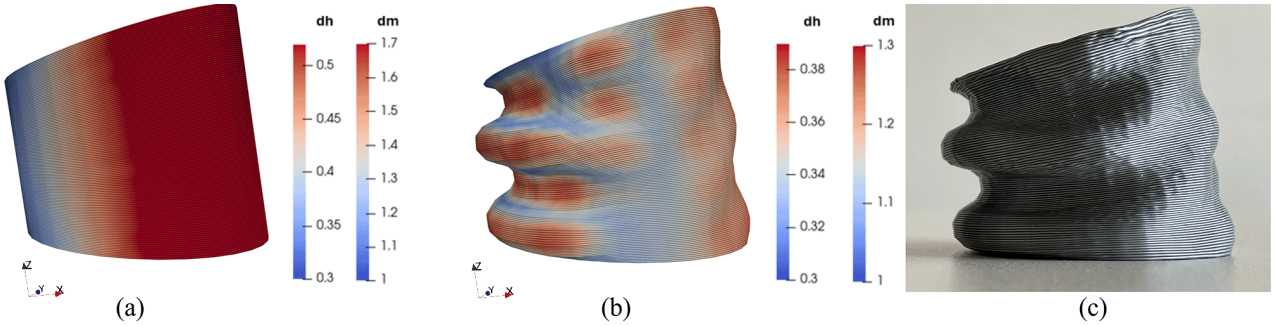

Figure 12: Results on the skewed cylinder for $\eta = 1.3$. Initial geometry (a) is outside the feasible layer-height range (unfeasible). After the optimization (b) $dm < \eta$ everywhere (feasible) and can be printed (c).

6 CREDITS

The co-first authors, F. Schito and J.D. Meza Zeron, equally contributed to this paper, which has been funded by BMW AG and the TUM Georg Nemetschek Institute.

REFERENCES

[1] E. Ulu, N. Gecer Ulu, W. Hsiao, and S. Nelaturi, "Manufacturability oriented model correction and build direction optimization for additive manufacturing," *Journal of Mechanical Design*, vol. 142, no. 6, p. 062001, 2020.

[2] J. Olsen and I. Y. Kim, "Design for additive manufacturing: 3d simultaneous topology and build orientation optimization," *Structural and Multidisciplinary Optimization*, vol. 62, no. 4, pp. 1989–2009, 2020.

[3] V. Mishra, C. Ayas, M. Langelaar, and F. Van Keulen, "Simultaneous topology and deposition direction optimization for wire and arc additive manufacturing," *Manufacturing Letters*, vol. 31, pp. 45–51, 2022.

[4] X. Chen, G. Fang, W.-H. Liao, and C. C. Wang, "Field-based toolpath generation for 3d printing continuous fibre reinforced thermoplastic composites," *Additive Manufacturing*, vol. 49, p. 102470, 2022.

[5] O. Stein, "A quick introduction to the laplacian and bilaplacian through the theory of partial differential equations," in *SGP 2021 Graduate School*, 2021.